ADVANCED MATERIALS
www.advmat.de

Nitrogen and Sulfur Codoped Graphene: Multifunctional Electrode Materials for High-Performance Li-Ion Batteries and Oxygen Reduction Reaction

Wei Ai, Zhimin Luo, Jian Jiang, Jianhui Zhu, Zhuzhu Du, Zhanxi Fan, Linghai Xie, Hua Zhang, Wei Huang, and Ting Yu**

Since the release of the first commercial prototype by the Sony Corporation in 1991, lithium-ion batteries (LIBs) have rapidly dominated the rechargeable battery market for portable electronics owing to their high energy density and environmental benignity.[1] In response to the ever-increasing consumption of fossil fuels and global pollution, the applications of LIBs are expanding to a wider range, particularly to electric vehicles and smart grids to achieve a sustainable world.[2] To match the momentum of vigorous development in both portable electronics and electric vehicles/smart grids, LIBs with improved energy capacity, rate capability, and structural stability are still required. So far, graphite has been the most widely used anode material for commercial LIBs owing to its benefits of low working voltage (vs. Li/Li^+), long-term cycling performance, high coulombic efficiency, and relative ease of preparation.[3] However, limited Li storage capacity, corresponding to the first-stage lithium graphite intercalation compound with stoichiometry LiC_6, and poor rate capability induced by its low Li diffusion coefficient are two main obstacles that impede further progress of graphite electrode materials.

Graphene, a single layer of graphite, exhibits many advantages, such as fascinating structure and electronic properties, overall chemical inertness, and relative ease of preparation when used as an anode material for LIBs.[4] In addition, advanced modifications of graphene can lead to a definitely enhanced electrochemical performance since the Li storage capability mainly depends on the structure and morphology of the anode material.[5] Both theoretical calculation and experimental results have proved that the introduction of N, P, S, or B atoms into graphene is generally effective in improving its electrical properties and chemical activity, which is very favorable for energy storage.[6] Currently, two main synthetic routes are used to fabricate heteroatom-doped graphene materials. One is the post-treatment of graphene precursors (e.g., graphene oxide (GO), exfoliated graphene) with reactive heteroatom sources such as triphenylphosphine,[6d] ionic liquids,[7] borane,[6b] and ammonia.[8] The other approach is the chemical vapor deposition (CVD) or pyrolysis of heteroatom- and carbon-containing precursors (e.g., pyridine, heteroatom-containing polymers) to directly incorporate heteroatoms into the carbon backbone.[9] Unfortunately, owing to the inevitable aggregation of graphene sheets and low content of doped atoms, the modified graphene materials have made limited progress in their Li storage performance, especially for the P, S, and B species. Therefore, to further improve the LIBs' performance, effective methods of doping graphene with two heteroatoms need to be proposed urgently because Li storage is determined not only by the number of heteroatoms but also by synergistic effects between dopants.[5b] Instead of increasing the doping level of a single heteroatom, it is possible to codope graphene with two different heteroatoms, which is a promising option for LIB applications that takes advantage of the additionally created defect sites for Li storage.

In this Communication, we report a novel approach to the synthesis of N- and S-codoped graphene (NS-G) through covalent functionalization of GO that uses 2-aminothiophenol (ATP) as a source of both N and S, followed by thermal treatment. Benefiting from the unique structural features and synergistic effects of N and S codoping, the resultant NS-G is demonstrated to be a superior anode material for LIBs in terms of super-high reversible capacity and excellent rate capability,

W. Ai, Dr. J. Jiang, J. H. Zhu, Prof. T. Yu
Division of Physics and Applied Physics
School of Physical and Mathematical Sciences
Nanyang Technological University
Singapore 637371, Republic of Singapore
E-mail: yuting@ntu.edu.sg
Dr. Z. M. Luo, Z. X. Fan, Prof. H. Zhang
School of Materials Science and Engineering
Nanyang Technological University
Singapore 639798, Republic of Singapore
Z. Z. Du, Prof. W. Huang
Jiangsu-Singapore Joint Research Center for Organic/Bio-Electronics & Information Displays and Institute of Advanced Materials (IAM)
Nanjing Tech University
30 South Puzhu Road, Nanjing 211816, Jiangsu, P. R. China
E-mail: iamwhuang@njtech.edu.cn
Prof. L. H. Xie, Prof. W. Huang
Key Laboratory for Organic Electronics & Information Displays and Institute of Advanced Materials (IAM)
Nanjing University of Posts and Telecommunications
9 Wenyuan Road, Nanjing 210023, Jiangsu, P. R. China
Prof. T. Yu
Graphene Research Centre
National University of Singapore
Singapore 117546, Republic of Singapore
Prof. T. Yu
Department of Physics
Faculty of Science
National University of Singapore
Singapore 117542, Republic of Singapore

DOI: 10.1002/adma.201401427

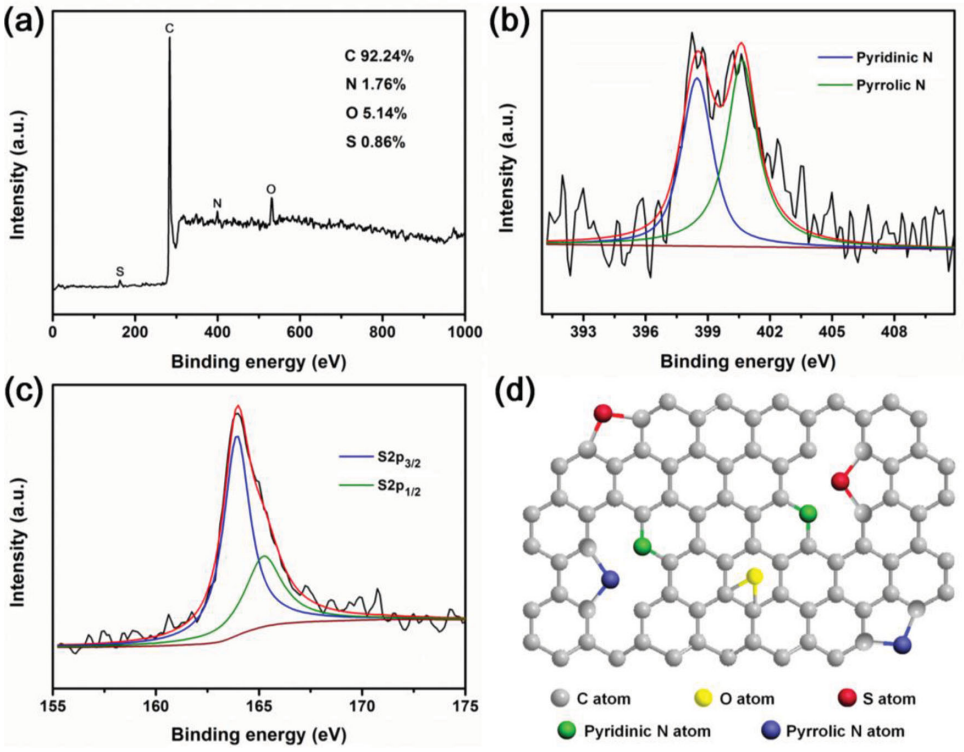

Figure 1. a) XPS survey spectrum of NS-G. b,c) High-resolution N 1s (b) and S 2p (c) XPS spectra of NS-G. d) Schematic illustration of the structure of NS-G.

as well as long-term cycling performance. Moreover, beyond applications in LIBs, our NS-G is also a promising candidate for other applications, such as supercapacitors, metal-free electrocatalysts, photocatalysts, and lithium-air batteries. As a proof of concept, NS-G has also been used as a metal-free catalyst for the oxygen reduction reaction (ORR), as which it also exhibits good electrocatalytic performance, indicating the huge potential of our NS-G.

The following three steps are involved in the synthesis of NS-G: i) the introduction of N and S atoms onto graphene sheets by means of a polyphosphoric acid–catalyzed cyclization process, ii) reduction of functionalized GO by N_2H_4 to remove the oxygen functional groups, and iii) subsequent calcination at 650 °C to obtain the final NS-G (Scheme S1, Supporting Information). X-ray photoelectron spectroscopy (XPS) measurements were performed to investigate the elemental composition and chemical status of the elements in NS-G. The XPS survey spectrum of NS-G (**Figure 1**a) shows four characteristic peaks located at ca. 164, 285, 399, and 532 eV, corresponding respectively to S 2p, C 1s, N 1s, and O 1s.[10] The elemental content of N and S in NS-G is 1.76% and 0.86%, respectively. For the reduced graphene oxide (rGO) (prepared under the same conditions except for the absence of ATP in step (i), see Figure S1, Supporting Information), no N and S signals were recorded, verifying the successful incorporation of N and S atoms into the graphene sheets. The high-resolution spectrum of C 1s in rGO and NS-G could be fitted by several peaks; both samples display peaks corresponding to C–C (284.6 eV), C–O (286.7 eV), C=O (288.0 eV), and O–C=O (289.2 eV), while for the NS-G sample, the particular peak located at 285.6 eV suggests the presence of C–S and C–N (Figure S2, Supporting Information).[11] Moreover, the high-resolution N 1s spectrum of NS-G reveals the presence of both pyridine-like N (398.5 eV) and pyrrole-like N (400.6 eV) species (Figure 1b),[12] whereas the S 2p spectrum of NS-G reveals the formation of thiophene-like structures between sulfur atoms and their neighboring carbon atoms due to spin–orbit coupling. Figure 1C shows that two peaks with an intensity ratio of 2:1 are present at 163.9 and 165.2 eV, agreeing well with S $2p_{3/2}$ and S $2p_{1/2}$.[13] Based on the above characterizations, we devised the structural scheme of NS-G illustrated in Figure 1d.

Further structural information about NS-G can be obtained from X-ray diffraction (XRD), Fourier-transform infrared (FTIR) spectra, and Raman spectra measurements. In XRD patterns (Figure S3, Supporting Information), GO has a diffraction peak at $2\theta = 9.98°$, corresponding to an interlayer spacing of 0.885 nm, arising from the intercalation of oxygen-containing functional groups between graphene sheets,[14] whereas rGO exhibits a well-defined peak at 26.3°, corresponding to an interlayer spacing of 0.339 nm, and NS-G exhibits a broader peak at 25.6° with a larger interlayer spacing of 0.348 nm. These results are in excellent agreement with the high-resolution transmission electron microscopy (HRTEM) data shown in Figure S4 (Supporting Information). Notably, the broadened full width at half maximum and the evidently decreased intensity imply a low graphitization degree of NS-G. In the FTIR spectra of rGO and NS-G (Figure S5a, Supporting Information), the peaks related to the oxygen-containing functional groups have almost totally disappeared, suggesting the successful removal of the oxygen groups on the graphene sheets. Raman spectra

Adv. Mater. **2014**,
DOI: 10.1002/adma.201401427

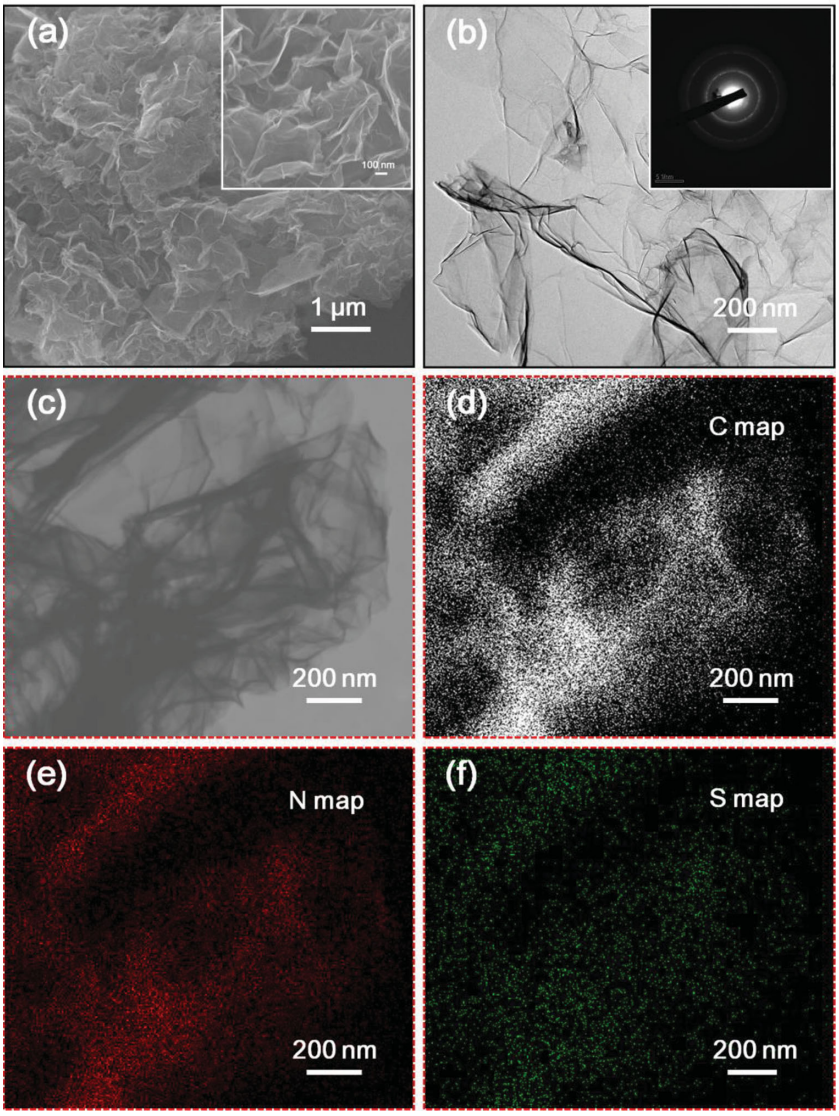

Figure 2. a) SEM image of NS-G. Inset: Higher-magnification SEM image of NS-G. b) TEM image of NS-G. Inset: Corresponding SAED pattern of NS-G. c) STEM image of NS-G with the corresponding carbon (d), nitrogen (e), and sulfur (f) elemental mapping images.

(Figure S5b, Supporting Information) of all three samples show two remarkable peaks around 1594 and 1348 cm^{-1}. The G band located at 1594 cm^{-1} is attributed to the first-order scattering of the E_{2g} mode of sp^2 carbon atoms while the D band at 1348 cm^{-1} is induced by defects or disorder. Moreover, the intensity ratio (I_D/I_G) of the D and G bands of GO, rGO, and NS-G are 0.99, 1.05, and 1.16, respectively. The increase of I_D/I_G is due to the formation of defects in graphene sheets,[15] further confirming the successful doping of N and S atoms.

Field-emission scanning electron microscopy (FESEM) and transmission electron microscopy (TEM) images (**Figure 2**a,b) reveal that ultrathin crumpled graphene sheets are randomly aggregated and overlapped with each other, forming an interconnected network in the porous NS-G. From the selected area electron diffraction (SAED) pattern (inset of Figure 2b), we conclude that NS-G is disordered, highly consistent with previous XRD and Raman results. In contrast, rGO shows a restacked graphite structure (Figure S6, Supporting Information) owing to the strong π-π stacking and van der Waals interactions between graphene sheets. Moreover, scanning transmission electron microscopy (STEM) elemental mapping of NS-G illustrates a homogeneous distribution of N and S atoms in graphene sheets (Figure 2c-f). The surface area of NS-G determined by Brunauer–Emmett–Teller (BET) measurements using N_2 adsorption–desorption analysis was 153 $m^2\ g^{-1}$ (Figure S7, Supporting Information). The close-to type IV N_2 adsorption–desorption isotherm with a clear hysteresis loop illustrates the coexistence of micropores (<2 nm) and mesopores (2–50 nm) in NS-G.[16] This was confirmed by further pore-size distribution analysis, revealing that NS-G has a multiple pore structure with average pore size of 6.4 nm.

Electrochemical Li storage properties of NS-G were evaluated in detail using the standard half-cell configuration. For comparison, the performance of the rGO electrode was also tested under the same electrochemical conditions. **Figure 3**a and Figure S8 (Supporting Information) show cyclic voltammetry (CV) curves of NS-G and rGO electrodes, which are consistent with those of previously reported carbon-based anode materials.[6d] In the first cycle, a pronounced reduction peak between 1.0 and 0.29 V is due to the formation of a solid electrolyte interphase (SEI) on the surface of the electrode.[17] The CV curves overlapped in the following cycles, indicative of formation of a stable SEI layer. The capacity below 0.5 V is ascribed to intercalation of the Li ions into the graphene layers, whereas the capacity above 0.5 V is attributed to the faradic capacitance on the surface or edge sites of graphene layers.[18] Figure 3b shows charge/discharge profiles of the NS-G and rGO electrodes at a current density of 200 mA g^{-1} between 0.005 and 3.0 V (vs. Li/Li^+). The initial discharge capacity for NS-G is 1636 mAh g^{-1} with a coulombic efficiency of 44.7%, much higher than the value for rGO (817 mAh g^{-1}). The large irreversible capacity in the first cycle was assigned to the formation of the SEI layer, as observed by previous CV curves. However, the coulombic efficiency increases dramatically upon cycling, reaching over 86% in the second cycle and over 98% after the following cycles. The cyclic performance of NS-G and rGO electrodes was investigated at a current rate of 200 mA g^{-1}, as shown in Figure 3c and Figure S9 (Supporting Information). The NS-G electrode still delivers a reversible capacity of 1090 mAh g^{-1} after 500 cycles, more than two times that of rGO (420 mAh g^{-1}). Notably, the capacity of the NS-G electrodes decreases in the first 20 cycles but then gradually increases upon cycling. The increase of

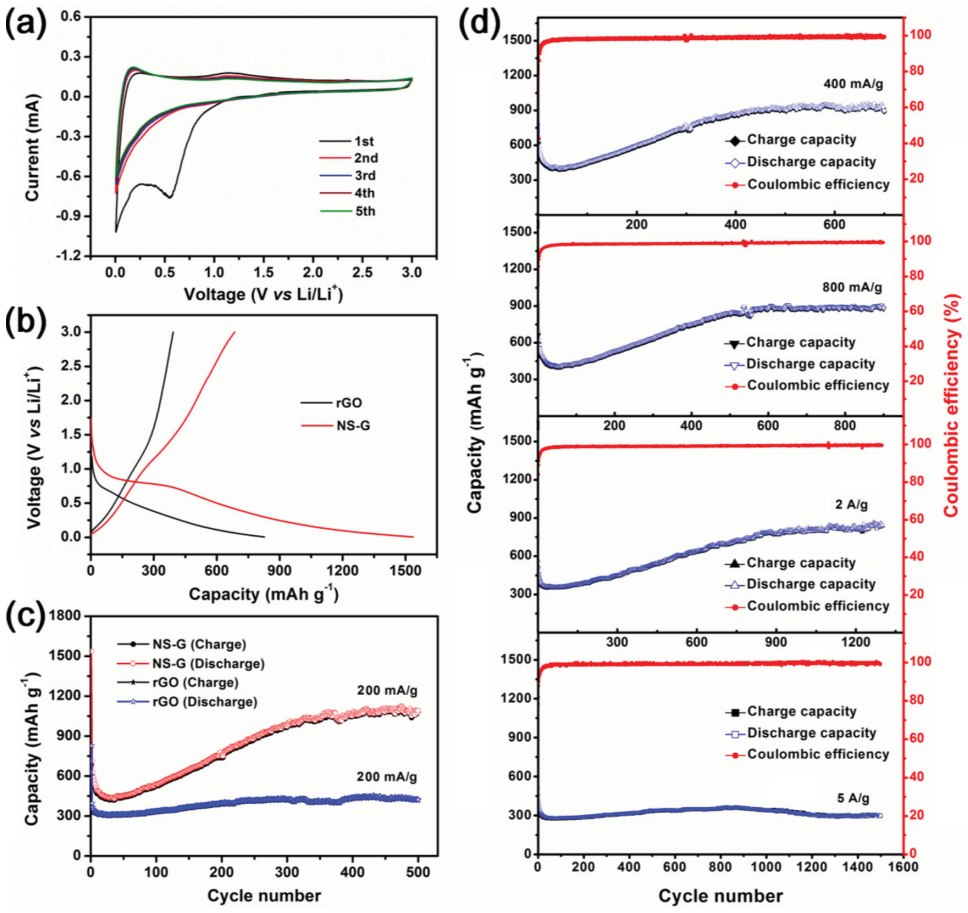

Figure 3. Electrochemical Li storage performance of rGO and NS-G. a) CV curves of the NS-G electrode at a sweep rate of 0.5 mV s^{-1}. b) Initial galvanostatic charge–discharge voltage versus capacity profiles of the rGO and NS-G electrodes at a current density of 200 mA g^{-1}. c) Cycling performance of the rGO and NS-G electrodes at a current density of 200 mA g^{-1}. d) Rate capability of the NS-G electrode at different rates.

capacity may be attributed to the improved access of Li ions into the inner part of porous NS-G upon cycling, which leads to an increased accommodation behavior for Li.[6c,19] Meanwhile, the enhanced conductivity of the NS-G electrode, demonstrated by electrochemical impedance spectroscopy (EIS; Figure S10, Supporting Information) could also be responsible for such capacity enhancement. Figure 3d shows the rate capability of the NS-G electrode at various current densities in comparison with the rGO electrode (Figure S11, Supporting Information). The NS-G material can sustain high capacities of 896, 882, 844, and 297 mAh g^{-1} with coulombic efficiency over 99% at current densities of 400, 800, 2000, and 5000 mA g^{-1}, respectively, even after 700, 900, 1300, and 1500 cycles. These values are much higher than for rGO, and also for reported graphene-based materials.[6d,20] EIS measurements were also carried out on the rGO and NS-G electrodes in the frequency range 1×10^5–0.01 Hz. Nyquist plots and the corresponding equivalent circuit are shown in Figure S12 (Supporting Information). The fitted data reveal that the NS-G electrode has a lower electrolyte resistance (R_S = 4.5 Ω) and charge transfer resistance (R_{CT} = 35 Ω) than the rGO electrode (R_S = 6.1 Ω, R_{CT} = 59 Ω).

The superior electrochemical performance of NS-G benefits from the unique structural features and the synergistic effects of N and S codoping in graphene.[21] From the above results, the interconnected graphene network formed by the random aggregation of crumpled graphene sheets can serve as continuous channels for electron transportation, whereas doping-induced topological defects together with the as-formed micropores and mesopores can act as the reservoirs for Li storage.[6d,19] Moreover, the ultrathin 2D structure of the NS-G shortens the solid-state diffusion length for Li ions, and also ensures high Li storage by utilizing both sides of the graphene sheets.[22] On the other hand, the large surface area provides sufficient contact areas between the electrode and electrolyte, facilitating rapid diffusion of Li ions within the electrode material, while the increased interlayer spacing facilitates the fast kinetics of Li intercalation.[23] In addition, owing to the differences in size and electronegativity between the doped N and S atoms on the one hand and carbon on the other, structural distortion and changes of the charge density are induced in the graphene sheet. This not only results in increased conductivity but also causes a large number of topological defects on the graphene sheet, which finally leads to the enhanced electrochemical activity.[5b,6d]

In addition to LIBs, the as-obtained NS-G may be valuable for other applications (e.g., supercapacitors, metal-free

Adv. Mater. 2014,
DOI: 10.1002/adma.201401427

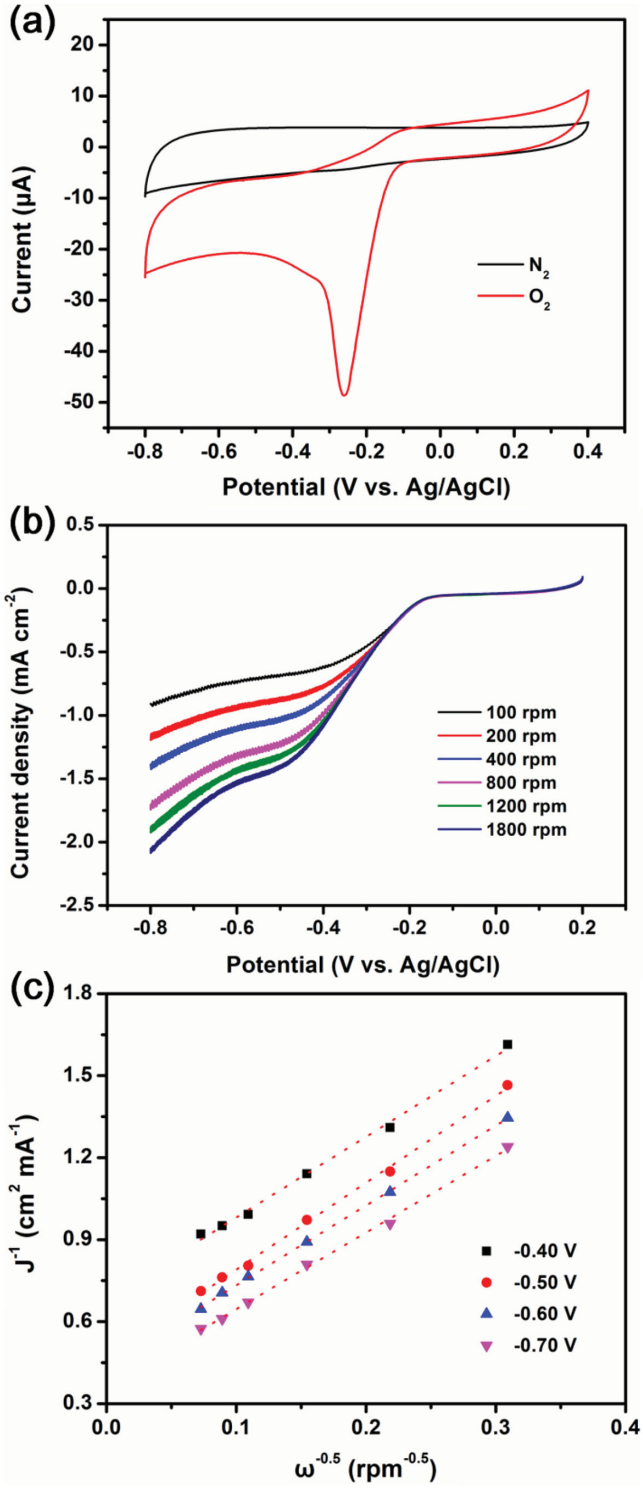

Figure 4. Electrochemical ORR catalytic performance of NS-G. a) CV curves of NS-G in N_2- and O_2-saturated 0.1 M KOH at a sweep rate of 10 mV s^{-1}. b) LSV of NS-G at different rotation rates. c) Koutecky-Levich plots at different potentials for NS-G.

electrocatalysts, photocatalysts, and lithium-air batteries) as well. As a proof of concept, we further investigated its electrocatalytic activity for ORR in an alkaline medium (**Figure 4** and Figure S13, Supporting Information). Figure 4a shows CV curves of NS-G in N_2- and O_2-saturated 0.1 M KOH at a sweep rate of 10 mV s^{-1}. A well-defined cathodic peak (reduction process) occurring at –0.26 V was observed in the O_2-saturated 0.1 M KOH solution. In contrast, only a quasi-rectangular voltammogram without any evident peaks was recorded in the same potential range in N_2-saturated KOH solution, owing to the supercapacitance property of porous carbon electrodes. The onset potential for ORR is more positive than for other recently reported metal-free ORR catalysts, such as N- and S-doped graphene, N-doped graphene composite, and N-doped graphene quantum dots (Table S1, Supporting Information),[24] indicating a pronounced electrocatalytic activity of the as-obtained NS-G for oxygen reduction. To gain further insight into the ORR process on NS-G, linear sweep voltammetry (LSV) measurements were carried out on a rotating disk electrode at various rotation speeds in O_2-saturated 0.1 M KOH solution at a scanning rate of 10 mV s^{-1} (Figure 4b). The diffusion-limited current density of oxygen reduction shows a typical increase as the rotation rate changes from 100 to 1800 rpm owing to the enhanced diffusion of electrolyte.[24a] Figure 4c shows the corresponding Koutecky–Levich plots at different potentials, and the good linearity of the plots implies a first-order reaction with respect to the dissolved oxygen concentration.[24c] The number of electrons transferred per oxygen molecule involved in the ORR process that is calculated from the Koutecky–Levich equation is 2.9–3.2 at potentials ranging from –0.4 to –0.7 V, suggesting both two-electron and four-electron procedures for oxygen reduction. The good electrocatalytic performance is attributed to the doped N and S atoms having different electronegativity (N: 3.04, S: 2.58) than carbon (2.55), which makes the graphene sheets non-electroneutral with many charged sites that are favorable for O_2 adsorption and its reduction,[10] while the synergistic effect of N and S codoping can create new non-electroneutral sites for electrochemical reaction.

In summary, we have developed a novel methodology for the synthesis of NS-G by means of covalent functionalization of GO followed by thermal treatment. The unique structural properties and synergistic effects of N and S codoping make NS-G a superior anode material for LIBs in terms of super-high reversible capacity, excellent rate capability and long-term cycling performance. As evidence of its multifunctional applications, NS-G was further employed as a metal-free catalyst for ORR, as which it also exhibited good electrocatalytic performance. Our method could be easily extended to the other carbon-based materials (e.g., porous carbons, carbon nanofibers, carbon nanotubes, etc.), which may shed light on the synthesis of doped carbon-based materials for future applications.

Experimental Section

Synthesis of GO: GO was synthesized from natural graphite by a modified Hummers' method, which has been reported previously.[25]

Synthesis of NS-G: GO solution (2 mg mL^{-1}) was prepared by ultrasonic exfoliation of graphite oxide (800 mg) in deionized water (400 mL) for 50 min; the solution was centrifuged at 1000 rpm for 10 min to remove the unexfoliated particles. After that, 2-aminothiophenol (3 mL) was added to the solution and sonicated for another 5 min. Then polyphosphoric acid (5 mL) was added dropwise under vigorous stirring,

and the solution was refluxed at 80 °C in the dark for 24 h. The product was collected by filtration and washing (ethanol and then water, 4 times each), then redispersed into deionized water (400 mL) by sonication for 5 min. Afterwards, hydrazine monohydrate (3 mL) was added and refluxed at 80 °C for 24 h. The as-obtained product was filtered and washed with deionized water for several times, then dried in vacuum at 120 °C for 12 h. Finally, the product was placed in the center of a quartz tube furnace. The system was heated to 650 °C (a higher calcination temperature will result in lower heteroatom doping level, while lower calcination temperature will lead to a low degree of graphitization) with a heating rate of 5 °C min^{-1} under nitrogen flow, kept at 650 °C for 30 min, and then allowed to cool down naturally.

Synthesis of rGO: rGO was synthesized by chemical reduction of exfoliated GO by hydrazine.[26] Typically, 2 mg mL^{-1} GO solution (100 mL) was prepared by ultrasonic exfoliation of graphite oxide in deionized water. Then hydrazine hydrate (0.75 mL) was added and the mixture was kept at 80 °C for 24 h. The product was collected by filtration, washed with deionized water several times, and dried under vacuum. For comparison, the as-obtained rGO was also calcined under the same thermal annealing conditions as NS-G.

Characterization: XPS analysis was performed on an ESCALAB MK II X-ray photoelectron spectrometer with a monochromatic Al Kα X-ray source. FESEM analysis was conducted with a JEOL JSM-6700F electron microscope with an accelerating voltage of 10 kV. TEM measurements were conducted on a JEOL JEM-2010 transmission electron microscope with an accelerating voltage of 200 kV. STEM and elemental mapping characterizations were carried out on a JEOL JSM-7600F microscope. XRD patterns were recorded on a D8 Advanced diffractometer with Cu Kα radiation (wavelength $\lambda = 1.54056$ Å). FTIR spectra were recorded on a NEXUS 670 FTIR spectrometer using KBr disks. Raman spectra were collected using a WITEC CRM200 Raman system using laser excitation at 532 nm. The nitrogen adsorption/desorption analysis was performed at 77 K on a Micromeritics ASAP 2020 instrument.

Electrochemical measurements: Li storage tests were carried out in 2032 coin-type cells assembled inside an argon-filled glove box with both moisture and oxygen contents below 0.1 ppm. The working electrodes were prepared by casting the slurry containing 80% active material, 10% acetylene black, and 10% poly(vinylidene fluoride) onto a copper foil current collector. Then they were dried in a vacuum oven at 100 °C for 12 h to remove the solvent. Pure lithium foil was used as the counter electrode. 1 M $LiPF_6$ solution in a 50:50 (w/w) mixture of ethylene carbonate and dimethyl carbonate served as the electrolyte. The galvanostatic charge–discharge tests were performed using a Neware battery testing system in the voltage range 0.005–3.0 V (vs. Li/Li^+). CV (0.005–3 V, 0.5 mV s^{-1}) and EIS measurements were carried out on a CHI 760D electrochemical workstation.

ORR measurements were performed on the CHI 760D electrochemical workstation using a conventional three-electrode system with Pt wire and Ag/AgCl as the counter and reference electrodes, respectively. The working electrodes were prepared by casting 5 μL of the catalyst ink (5 mg mL^{-1}) onto the prepolished glassy carbon disk electrodes (3.0 mm in diameter).[27] The ORR tests were carried out in O_2-saturated 0.1 M KOH solution. LSV measurements were conducted with a scan rate of 10 mV s^{-1} at different rotation rates from 100 to 1800 rpm.

Supporting Information

Supporting Information is available from the Wiley Online Library or from the authors.

Acknowledgements

This work is supported by the Singapore National Research Foundation under NRF RF Award no. NRFRF2010–07, A*Star SERC PSF grant 1321202101, and MOE Tier 2 MOE2012-T2–2–049. H.Z. is grateful for the support from Singapore MOE under AcRF Tier 2 (ARC 26/13, no. MOE2013-T2–1–034) and AcRF Tier 1 (RG 61/12), and the Start-Up Grant (M4080865.070.706022) in NTU. This research is also funded by the Singapore National Research Foundation and the publication is supported under the Campus for Research Excellence and Technological Enterprise (CREATE) programme (Nanomaterials for Energy and Water Management).

Received: March 30, 2014
Revised: June 25, 2014
Published online:

[1] a) T. Nagaura, K. Tozawa, *Prog. Batteries Solar Cells.* **1990**, *9*, 209; b) T. Nagaura, *Prog. Batteries Solar Cells.* **1991**, *10*, 218.
[2] J. B. Goodenough, K. S. Park, *J. Am. Chem. Soc.* **2013**, *135*, 1167.
[3] N. A. Kaskhedikar, J. Maier, *Adv. Mater.* **2009**, *21*, 2664.
[4] Y. Sun, Q. Wu, G. Shi, *Energy Environ. Sci.* **2011**, *4*, 1113.
[5] a) T. Bhardwaj, A. Antic, B. Pavan, V. Barone, B. D. Fahlman, *J. Am. Chem. Soc.* **2010**, *132*, 12556; b) J. P. Paraknowitsch, A. Thomas, *Energy Environ. Sci.* **2013**, *6*, 2839.
[6] a) A. L. M. Reddy, A. Srivastava, S. R. Gowda, H. Gullapalli, M. Dubey, P. M. Ajayan, *ACS Nano* **2010**, *4*, 6337; b) Z. S. Wu, W. Ren, L. Xu, F. Li, H. M. Cheng, *ACS Nano* **2011**, *5*, 5463; c) W. Ai, L. Xie, Z. Du, Z. Zeng, J. Liu, H. Zhang, Y. Huang, W. Huang, T. Yu, *Sci. Rep.* **2013**, *3*, 2341; d) C. Zhang, N. Mahmood, H. Yin, F. Liu, Y. Hou, *Adv. Mater.* **2013**, *25*, 4932.
[7] P. Bhunia, E. Hwang, Y. Yoon, E. Lee, S. Seo, H. Lee, *Chem. Eur. J.* **2012**, *18*, 12207.
[8] X. Li, H. Wang, J. T. Robinson, H. Sanchez, G. Diankov, H. Dai, *J. Am. Chem. Soc.* **2009**, *131*, 15939.
[9] a) Z. Jin, J. Yao, C. Kittrell, J. M. Tour, *ACS Nano* **2011**, *5*, 4112; b) B. Guo, X. G. Sun, G. M. Veith, Z. Bi, S. M. Mahurin, C. Liao, C. Bridges, M. P. Paranthaman, S. Dai, *Adv. Energy Mater.* **2013**, *3*, 708.
[10] J. Liang, Y. Jiao, M. Jaroniec, S. Z. Qiao, *Angew. Chem. Int. Ed.* **2012**, *51*, 11496.
[11] Y. Dong, H. Pang, H. B. Yang, C. Guo, J. Shao, Y. Chi, C. M. Li, T. Yu, *Angew. Chem. Int. Ed.* **2013**, *52*, 7800.
[12] W. Ai, W. Zhou, Z. Du, Y. Du, H. Zhang, X. Jia, L. Xie, M. Yi, T. Yu, W. Huang, *J. Mater. Chem.* **2012**, *22*, 23439.
[13] J. P. Bearinger, S. Terrettaz, R. Michel, N. Tirelli, H. Vogel, M. Textor, J. A. Hubbell, *Nat. Mater.* **2003**, *2*, 259.
[14] S. Song, Y. Xue, L. Feng, H. Elbatal, P. Wang, C. N. Moorefield, G. R. Newkome, L. Dai, *Angew. Chem. Int. Ed.* **2014**, *53*, 1415.
[15] C. N. R. Rao, A. K. Sood, K. S. Subrahmanyam, A. Govindaraj, *Angew. Chem. Int. Ed.* **2009**, *48*, 7752.
[16] Y. Tao, H. Kanoh, L. Abrams, K. Kaneko, *Chem. Rev.* **2006**, *106*, 896.
[17] W. H. Shin, H. M. Jeong, B. G. Kim, J. K. Kang, J. W. Choi, *Nano Lett.* **2012**, *12*, 2283.
[18] E. Yoo, J. Kim, E. Hosono, H. S. Zhou, T. Kudo, I. Honma, *Nano Lett.* **2008**, *8*, 2277.
[19] L. Qie, W. M. Chen, Z. H. Wang, Q. G. Shao, X. Li, L. X. Yuan, X. L. Hu, W. X. Zhang, Y. H. Huang, *Adv. Mater.* **2012**, *24*, 2047.
[20] Y. Fang, Y. Lv, R. Che, H. Wu, X. Zhang, D. Gu, G. Zheng, D. Zhao, *J. Am. Chem. Soc.* **2013**, *135*, 1524.
[21] a) X. Wang, X. Q. Cao, L. Bourgeois, H. Guan, S. M. Chen, Y. T. Zhong, D. M. Tang, H. Q. Li, T. Y. Zhai, L. Li, Y. Bando, D. Golberg, *Adv. Funct. Mater.* **2012**, *22*, 2682; b) C. Nethravathi, C. R. Rajamathi, M. Rajamathi, U. K. Gautam, X. Wang, D. Golberg, Y. Bando, *ACS Appl. Mater. Interfaces* **2013**, *5*, 2708; c) X. Wang, Q. H. Weng, X. Z. Liu, X. B. Wang, D. M. Tang, W. Tian, C. Zhang, D. Q. Liu, Y. Bando, D. Golberg, *Nano Lett.* **2014**, *14*, 1164.
[22] J. R. Dahn, T. Zheng, Y. Liu, J. S. Xue, *Science* **1995**, *270*, 590.

DOI: 10.1002/adma.201401427

[23] J. S. Park, M. H. Lee, I. Y. Jeon, H. S. Park, J. B. Baek, H. K. Song, *ACS Nano* **2012**, *6*, 10770.

[24] a) Y. Li, Y. Zhao, H. Cheng, Y. Hu, G. Shi, L. Dai, L. Qu, *J. Am. Chem. Soc.* **2011**, *134*, 15; b) S. Yang, L. Zhi, K. Tang, X. Feng, J. Maier, K. Müllen, *Adv. Funct. Mater.* **2012**, *22*, 3634; c) P. Chen, T. Y. Xiao, Y. H. Qian, S. S. Li, S. H. Yu, *Adv. Mater.* **2013**, *25*, 3192; d) Y. Z. Sua, Y. Zhang, X. D. Zhuang, S. Li, D. Q. Wu, F. Zhang, X. L. Feng, *Carbon* **2013**, *62*, 296.

[25] a) W. Ai, J. Q. Liu, Z. Z. Du, X. X. Liu, J. Z. Shang, M. D. Yi, L. H. Xie, J. J. Zhang, H. F. Lin, T. Yu, W. Huang, *RSC Adv.* **2013**, *3*, 45; b) W. Ai, Z. Z. Du, J. Q. Liu, F. Zhao, M. D. Yi, L. H. Xie, N. E. Shi, Y. W. Ma, Y. Qian, Q. L. Fan, T. Yu, W. Huang, *RSC Adv.* **2012**, *2*, 12204.

[26] S. Park, J. An, J. R. Potts, A. Velamakanni, S. Murali, R. S. Ruoff, *Carbon* **2011**, *49*, 3019.

[27] Z. Luo, L. Yuwen, B. Bao, J. Tian, X. Zhu, L. Weng, L. Wang, *J. Mater. Chem.* **2012**, *22*, 7791.